

Research



Cite this article: Karim ET, He M, Salhoumi A, Zhigilei LV, Galenko PK. 2021 Kinetics of solid–liquid interface motion in molecular dynamics and phase-field models: crystallization of chromium and silicon. *Phil. Trans. R. Soc. A* **379**: 20200320. <https://doi.org/10.1098/rsta.2020.0320>

Accepted: 20 April 2021

One contribution of 14 to a theme issue ‘Transport phenomena in complex systems (part 1)’.

Subject Areas:
materials science

Keywords:

kinetics of crystallization, solid–liquid interface, molecular dynamics, phase-field model

Authors for correspondence:

Leonid V. Zhigilei

e-mail: lz2n@virginia.edu

Peter K. Galenko

e-mail: peter.galenko@uni-jena.de

Electronic supplementary material is available online at <https://doi.org/10.6084/m9.figshare.c.5438807>.

Kinetics of solid–liquid interface motion in molecular dynamics and phase-field models: crystallization of chromium and silicon

Eaman T. Karim^{1,2}, Miao He², Ahmed Salhoumi³, Leonid V. Zhigilei² and Peter K. Galenko^{4,5}


¹Department of Innovation and Technology Research, American Dental Association Science and Research Institute, 100 Bureau Drive, Gaithersburg, MD 20899, USA

²Department of Materials Science and Engineering, University of Virginia, Charlottesville, VA 22904-4745, USA

³Faculty of Sciences Ben M'Sik, Department of Physics, Laboratory of Condensed Matter Physics (LPMC), University of Hassan II Casablanca, BP 7955 Casablanca, Morocco

⁴Otto Schott Institute of Materials Research, Physics–Astronomy Faculty, Friedrich Schiller University Jena, 07743 Jena, Germany

⁵Laboratory of Multi-scale Mathematical Modeling, Department of Theoretical and Mathematical Physics, Ural Federal University, 620000 Ekaterinburg, Russia

 ETK, 0000-0002-7077-5704; MH, 0000-0003-1023-1040; AS, 0000-0002-9288-1196; LVZ, 0000-0002-1549-7086; PKG, 0000-0003-2941-7742

The results of molecular dynamics (MD) simulations of the crystallization process in one-component materials and solid solution alloys reveal a complex temperature dependence of the velocity of the crystal–liquid interface featuring an increase up to a maximum at 10–30% undercooling below the equilibrium melting temperature followed by a gradual decrease of the velocity at deeper levels of undercooling. At the qualitative level, such non-monotonous behaviour of the crystallization front velocity is consistent with the diffusion-controlled crystallization process described by the Wilson–Frenkel model, where the almost linear increase of the interface velocity in the vicinity of melting temperature is defined by the growth

of the thermodynamic driving force for the phase transformation, while the decrease in atomic mobility with further increase of the undercooling drives the velocity through the maximum and into a gradual decrease at lower temperatures. At the quantitative level, however, the diffusional model fails to describe the results of MD simulations in the whole range of temperatures with a single set of parameters for some of the model materials. The limited ability of the existing theoretical models to adequately describe the MD results is illustrated in the present work for two materials, chromium and silicon. It is also demonstrated that the MD results can be well described by the solution following from the hodograph equation, previously found from the kinetic phase-field model (kinetic PFM) in the sharp interface limit. The ability of the hodograph equation to describe the predictions of MD simulation in the whole range of temperatures is related to the introduction of slow (phase field) and fast (gradient flow) variables into the original kinetic PFM from which the hodograph equation is obtained. The slow phase-field variable is responsible for the description of data at small undercoolings and the fast gradient flow variable accounts for local non-equilibrium effects at high undercoolings. The introduction of these two types of variables makes the solution of the hodograph equation sufficiently flexible for a reliable description of all nonlinearities of the kinetic curves predicted in MD simulations of Cr and Si.

This article is part of the theme issue 'Transport phenomena in complex systems (part 1)'.

1. Introduction

Kinetics of solid–liquid interface in metals and alloys was widely investigated experimentally [1–5], in molecular dynamics (MD) simulations [2,6–16], and theoretically, with the diffusion-limited theory (DLT) [17,18] and the collision-limited theory (CLT) [19,20]. Special attention has been devoted to the nonlinear [21] and often non-monotonous [2,6–16] temperature dependence of the crystal growth velocity during rapid solidification, which manifests itself at high thermodynamic driving force for the phase transformation [22–24]. It has been shown [25] that the traditional kinetic theories, such as CLT and DLT, as well as the phase-field models (PFMs) based on local thermodynamic equilibrium [26], often fail to quantitatively describe the nonlinear behaviour in the crystal growth velocity predicted in MD simulations. While the local equilibrium PFMs can describe the nonlinear dependence of the interface velocity predicted in MD simulations in a relatively narrow temperature range [27], the extension of this description to a wider range of undercoolings, where the velocity goes through the maximum and slows down with increasing undercooling [2,7–16], still presents a challenge.

A formulation of the PFM accounting for both slow variables evolving on the timescale of classical thermodynamic variables (e.g. internal energy, chemical potential and phase field) and fast variables with relaxation times typical of kinetic variables (e.g. fluxes and gradient flows) [28–30] allows us to combine local equilibrium and local non-equilibrium effects in the phase transformation occurring at low and high undercoolings, respectively. Using the sharp interface limit of the hyperbolic equation derived from the kinetic PFM, the Gibbs–Thomson-type equation has been obtained [31,32]. This equation has a form of the hodograph equation that relates the interface acceleration and velocity to the interface curvature and the driving force for the phase transformation. The interface velocity predicted by this equation has been shown to be in good agreement with the results of MD simulations performed for pure metals and alloys [25,32–35].

In the present work, we illustrate the ability of the kinetic PFM formulated in the form of the hodograph equation to provide an adequate description of the velocity of crystal–liquid interface predicted in MD simulations for two elemental systems with different crystal structures, namely, body-centred cubic (bcc) Cr and diamond cubic (dc) Si. For both systems, the MD simulations of steady-state propagation of the crystal–liquid interface predict the characteristic bell-shaped velocity–temperature curves exhibiting maxima at approximately $0.75T_m$ for Cr and approximately $0.85T_m$ for Si. The Wilson–Frenkel model based on consideration of the

diffusion-limited kinetics of the interface is found to provide an adequate description of the MD data for Si, albeit only when independently determined temperature dependences of the liquid phase atomic diffusivity and latent heat of melting are included. The Wilson-Frenkel model, however, cannot be consistently applied to the description of the MD results for Cr, where the activation energy associated with the mobility of atoms in the liquid phase has to be changed by more than a factor of three between the two branches of the bell-shaped interface velocity curve. In the absence of a unified theoretical description of the MD data, the phase-field solution of the hodograph equation provides an attractive alternative and is demonstrated to be capable of an accurate continuum-level description of the interface kinetics for both Cr and Si. While the results reported in this paper are promising, clear physical interpretation of the parameters and assumptions of the PFM requires further detailed analysis of the atomic-scale mechanisms controlling the mobility of the crystal–liquid interface.

2. Molecular dynamics simulation

(a) Computational method

Two series of MD simulations are performed for Cr and Si solid–liquid coexistence systems maintained at different temperatures and zero pressure. The interatomic interactions are described by the embedded atom method (EAM) potential parametrized for Cr [36] and the modified Tersoff potential for Si [37]. The two potentials provide computationally efficient yet sufficiently accurate descriptions of real Cr and Si, including lattice parameters, cohesive energy, elastic constants and their temperature dependences, and vacancy formation energies. The equilibrium melting temperatures, T_m , obtained from MD simulations performed for solid–liquid coexistence systems under conditions of constant zero pressure and defined as temperatures when the interface velocities reach zero, are 2332 K for EAM Cr [38] and 1681 K [37] for Si.

The temperature dependence of the velocity of solid–liquid interface is evaluated in MD simulations performed for solid–liquid coexistence systems with dimensions of about $3 \times 3 \times 100 \text{ nm}^3$ (70 000 atoms) and about $22 \times 22 \times 50 \text{ nm}^3$ (1 228 800 atoms) for Cr and Si, respectively. The computational systems, schematically illustrated in figure 1, consist of liquid and solid parts forming two interfaces perpendicular to the [001] direction in the cubic crystal structures. Periodic boundary conditions are applied in all three directions, so that a model system effectively represents a periodic arrangement of infinitely wide liquid and crystalline layers. The coexistence systems for Cr and Si are prepared using different procedures. For Cr, the procedure is illustrated in figure 1. The liquid layer within the initially fully crystalline system is generated by superheating the corresponding part of the system above the limit of thermodynamic stability of the crystalline material against the onset of homogeneous melting, approximately $1.2\text{--}1.3T_m$ [39,40], to induce rapid homogeneous melting. At the same time, another part of the system is maintained at a temperature slightly below the melting temperature to preserve the crystalline structure of the solid layer. Following this step, the coexistence systems are relaxed at the equilibrium melting temperature and then rapidly cooled to desired temperatures below T_m . For Si, the liquid and crystal parts are prepared and equilibrated at a desired temperature above or below T_m separately, in two independent simulations. The simulations are performed in systems having the same lateral (x and y) dimensions that correspond to zero pressure in the crystalline system at a desired temperature. The coexistence systems are then created by combining a 40 nm thick liquid slab with a 10 nm thick crystalline slab for simulation of crystallization and a 10 nm thick liquid slab with a 40 nm thick crystalline slab for simulation of melting.

The simulations of crystallization and, in the case of Si, melting are performed under conditions of constant zero pressure, maintained by scaling the system in the direction of the longest axis normal to the crystal–liquid interfaces using the Berendsen barostat algorithm [41]. The lateral sizes of the computational systems, in the directions parallel to the crystal–liquid interfaces, are fixed so that the lattice parameters in the crystalline parts are equal to the equilibrium values at the desired temperatures and zero pressure. In order to avoid the local

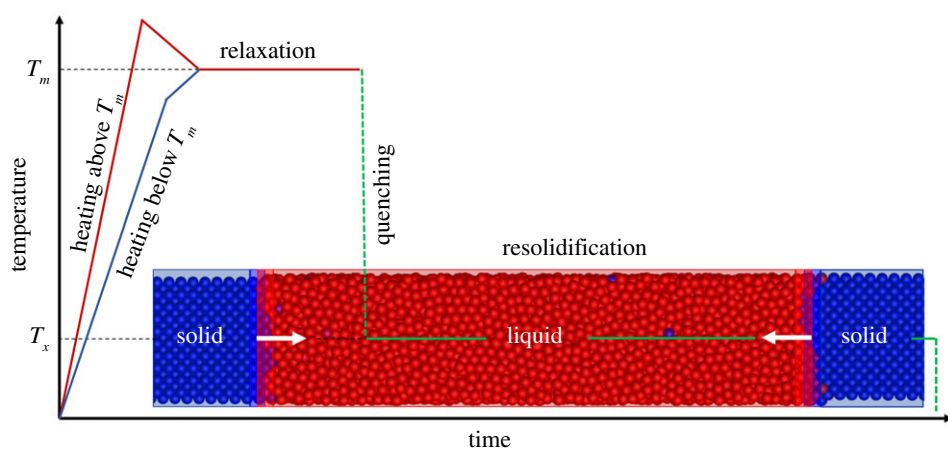


Figure 1. Schematic illustration of the thermal treatment used in the preparation of crystal–liquid coexistence systems for MD simulations of the crystallization process. The red line shows the thermal history of a part of the system that is heated above the T_m and undergoes melting. The blue line corresponds to a part of the system that is kept below T_m and preserves its crystalline state. The snapshot of an atomic system in the diagram represents a computational set-up for MD simulation of the crystallization process under controlled temperature, T_x , and zero pressure conditions. (Online version in colour.)

increase in the temperature at the rapidly advancing interface due to the release of the heat of melting [11,42,43], each system is divided into layers with thickness of 3 nm and 4 nm for Cr and Si, respectively, and the temperature is controlled through Berendsen thermostat algorithm [41] applied independently to each layer. This method eliminates the temperature variation across the length of the system and ensures that the temperature at the moving crystallization front is close to the nominal temperature T_x maintained in the simulation.

The crystallization front velocities are calculated in simulations of steady-state propagation of the two crystal–liquid interfaces present in the coexistence systems, as illustrated in figure 1. For Si, the crystal–liquid interface velocity is calculated as [44], $V = v_s \Delta v_{tot} / [2A_{xy}(v_s - v_l)\Delta t]$, where v_s and v_l are the average atomic volumes associated with the solid and liquid phases, respectively, at a temperature used in the simulation, Δv_{tot} is the change of the total volume of the crystal–liquid coexistence system during time period Δt , and A_{xy} is the cross-sectional area along the x – y plane parallel to the crystal–liquid interfaces. The factor of 2 in the denominator is due to the presence of two interfaces in the coexistence system. For the Cr system, the positions of the crystal–liquid interfaces are directly monitored every 5 ps by the following method. The atomic configurations generated in the course of a simulation are quenched for 1 ps using a velocity dampening technique, where the velocity of each individual atom is set to zero at the time when the kinetic energy of the atom maximizes. The fast quenching does not introduce any structural changes to the atomic configurations but makes the visualization and structural analysis more straightforward. The quenched systems are then divided into 700 layers parallel to the solid–liquid interface, so that each layer in the solid phase includes one atomic plane. The planes with crystalline ordering are identified based on structural analysis and potential energy of atoms, and the average positions of the two ordered atomic planes adjacent to the liquid phase are taken as the positions of the crystal–liquid interfaces. The velocity of the interface is evaluated by tracking the movement of the two liquid–crystal interfaces present in the coexistence systems [16].

The temperature dependence of the crystallization front velocity is evaluated in series of simulations performed at temperatures ranging from T_m down to $0.10T_m$ for Cr and from $0.95T_m$ down to $0.75T_m$ for Si. These temperature ranges are covered with an increment of $0.05T_m$ for these two systems. In total, the crystallization front velocities are evaluated in 17 simulations of Cr and 5 simulations of Si crystal–liquid coexistence systems. For the Si system,

three additional simulations are performed in the melting regime, at temperatures of $1.07T_m$, $1.13T_m$ and $1.19T_m$. All simulations, except those performed for Cr at $T = T_m$ and $T = 0.1T_m$, are continued until the complete crystallization or melting of the systems. We note that the onset of the homogeneous nucleation of new crystallites under conditions of deep undercooling down to approximately $0.7T_m$ and below, observed in earlier simulations performed for fcc metals [16], can potentially complicate the evaluation of the crystallization front velocity. While no homogeneous crystallization is observed in the simulations of Si, the homogeneous nucleation of small crystalline structures is detected inside the undercooled liquid phase in simulations of Cr performed at $0.60T_m$ and $0.65T_m$. Owing to the low fractions of these structures, however, they do not affect the velocity of the crystallization front in any significant way and do not prevent a reliable evaluation of the steady-state interface velocities at these temperatures.

The velocities of the solid–liquid interface obtained in the simulations are used for fitting the kinetic equation, as described in §2b. In order to define the standard deviation of the interface velocity data points, the simulations are repeated for each temperature three times for the Cr and four times for the Si system, with each simulation starting from different initial conditions. For Cr, the velocities of the two interfaces present in each coexistence system are evaluated independently. As a result, six and four independently calculated values of the interface velocity are obtained for each temperature for Cr and Si, respectively. These values are then used in the calculation of the standard deviations of the data points in the velocity–temperature dependences predicted in the MD simulations.

(b) Results of MD simulations

The temperature dependences of the solid–liquid interface velocity predicted in MD simulations of two model materials, Cr and Si, are shown in figure 2. In general, the two dependences exhibit some similarities, particularly at low to moderate levels of undercooling extending down to approximately $0.75T_m$ for Cr, and approximately $0.85T_m$ for Si. Within this range of temperatures, the crystallization front velocity increases with decreasing temperature in a similar manner for the two materials, reaching the maximum values of approximately 150 m s^{-1} for Cr and approximately 14 m s^{-1} for Si. With further temperature decrease, the initial increase of the interfacial velocity is followed by a steady decrease that brings the velocity down to the levels that cannot be resolved in an MD simulation at approximately $0.1T_m$ for Cr and approximately $0.7T_m$ for Si.

The temperature dependences of the crystal–liquid interface velocity obtained in this work for Cr and Si are consistent with the results of earlier MD simulations, where a gradual decrease of the velocity from the maximum value down to zero is reported for most of the bcc metals [7,12,13,16] and Si [14,15].

The temperature dependences of the crystallization velocity predicted in MD simulations of Cr cannot be consistently fitted to any single kinetic equation suggested for the description of the crystallization process [17,18,45–47]. Therefore, following an approach suggested in ref. [13], the velocity of the crystallization front is described here by two kinetic equations independently fitted in the lower and higher temperature regimes.

In the temperature range from T_m down to $0.7T_m$, the velocity of the crystallization front is described by the Wilson–Frenkel equation based on the phenomenological transition state theory that considers the exchange of atoms between the liquid and crystal phases at the interface [47]:

$$V(T) = C_h(T) \exp\left(\frac{-Q_h}{k_B T}\right) \left[1 - \exp\left(-\frac{\Delta G(T)}{k_B T}\right)\right], \quad (2.1)$$

where $\Delta G = G_l - G_s$ is the difference in the free energy of the solid and liquid phases, Q_h is the activation energy associated with the mobility of atoms in the liquid phase, k_B is the Boltzmann constant and C_h is a coefficient that depends on the interatomic spacing, the frequency of atomic vibrations, and the average thermal velocity of atoms in the liquid phase. The free energy difference is approximated as $\Delta G(T) \approx \Delta H_m(T_m - T)/T_m$, where ΔH_m is the latent heat

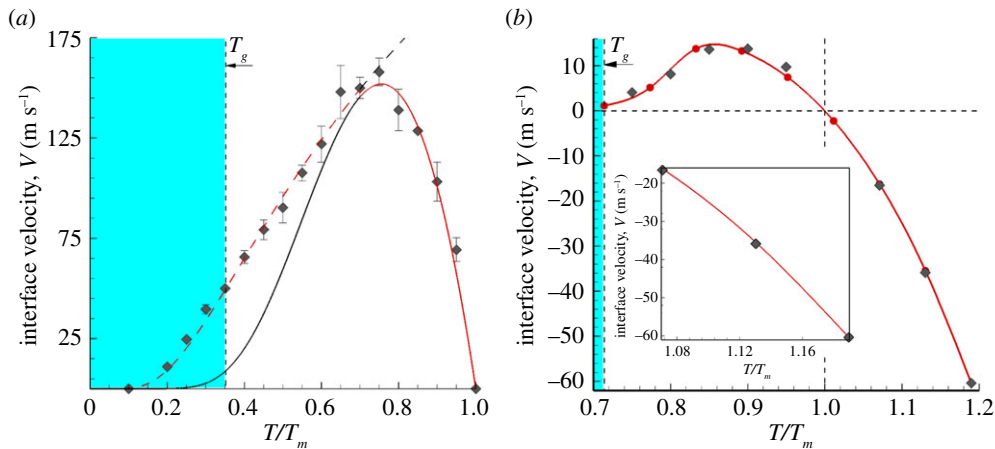


Figure 2. Crystal–liquid interface velocity versus normalized temperature predicted in MD simulations of EAM Cr (a) and modified Tersoff Si (b) crystal–liquid coexistence systems (dark diamonds). The light blue region on the left side of (a) and (b) in each diagram represent the amorphous state of the material, with the glass transition temperatures T_g determined for the two model materials as described in the text. The error bars represent the standard deviation obtained from the results of three and four sets of simulations performed for Cr and Si, respectively, each starting at different initial conditions. In (b), the error bars are comparable to the size of the symbols representing the data points and are not shown. In (a), the red solid and dashed lines represent the fitting of the MD results to equations (2.1) and (2.2), respectively, while the black parts of the solid and dashed lines correspond to the temperature ranges where the equations do not match the results of the simulations. The inset in (b) shows the data points for melting front propagation at $1.07T_m$, $1.13T_m$ and $1.19T_m$ used for fitting the pre-factor C_0 in equation (2.3). The velocities predicted by equation (2.3) are depicted by red circles connected by the red curve. The positive and negative values of the velocity correspond to crystallization and melting, respectively. (Online version in colour.)

of melting at T_m evaluated in a separate set of MD simulations performed for the liquid and solid EAM Cr ($\Delta H_m = 22.6 \text{ kJ mol}^{-1} = 0.234 \text{ eV atom}^{-1}$ [36]). The remaining two parameters of equation (2.1), determined by fitting to the data points in the range of $T_m > T > 0.7T_m$, are $C_h = 14\,013 \text{ m s}^{-1}$ and $Q_h = 0.511 \text{ eV}$ for the EAM Cr.

With these fitting parameters, equation (2.1) provides an adequate description of the close-to-linear increase of the interface velocities with decreasing temperature at small undercoolings, at $T < 0.9T_m$, where the crystal–liquid interface velocity is largely defined by the increase in the thermodynamic driving force for the phase transformation, $\Delta G(T)$. The nearly linear regime is followed by gradual weakening of the dependence and eventual transition through a maximum upon further increase of the undercooling, where the decrease in atomic mobility with increasing undercooling, accounted for by $\exp(-Q_h/k_B T)$ in equation (2.1), starts to dominate the temperature dependence. The maximum value of the interface velocity determined in MD simulations and the corresponding temperature of $0.75T_m$ for Cr is still described reasonably well by equation (2.1).

The decrease of the crystallization front velocity with further increase of the undercooling predicted by the equation, however, is substantially faster than that observed in MD simulations, as can be seen from the deviation of the data points from black solid curves in figure 2a. Given the inability of equation (2.1) to describe the interface velocities in the low-temperature regime, the results of the MD simulations at $T < 0.7T_m$ are fitted to a simple Arrhenius expression:

$$V(T) = C_l \exp\left(-\frac{Q_l}{k_B T}\right). \quad (2.2)$$

Fitting of equation (2.2) to the MD results yields values of $C_l = 453 \text{ m s}^{-1}$ and $Q_l = 0.156 \text{ eV}$ for Cr. While equation (2.2) can be considered as an approximation of equation (2.1) under

conditions of the large thermodynamic driving force, the more than threefold reduction of the apparent activation energy Q_l with respect to Q_h suggest that a consistent description of the crystallization kinetics in terms of thermally activated atomic rearrangements at the interface is not possible. The large drop of the effective activation energy observed for Cr points to a change in the dominant microscopic mechanisms responsible for the advancement of the crystallization front in the low-temperature regime, below $0.7T_m$.

The transition to the region with weaker, as compared to the prediction of the Wilson–Frenkel equation, temperature dependence of the crystallization front velocity is observed at the levels of undercooling approaching the glass transition temperature T_g . For the EAM Cr, $T_g = 810 \text{ K} = 0.35T_m$ is determined [48] from the temperature dependence of the second moment of the atomic-level hydrostatic stress distribution, following a method suggested in ref. [49]. Although, at the qualitative level, the sharp drop in the apparent activation energy in bcc Cr can be attributed to the limited relaxation of glass or deeply undercooled liquid in the vicinity of the crystallization front [13,50], a reliable predictive analytical model of the crystallization front propagation in the absence of full relaxation of the disordered phase is still lacking for this regime.

The temperature dependence of the solid–liquid interface velocity for Si, figure 2b, appears to be similar to that for Cr, featuring an increase of the solidification velocity with the degree of undercooling followed by a gradual decrease down to zero at approximately $0.7T_m$, when Si turns into an amorphous state. The maximum solidification front velocity of Si, approximately 14 m s^{-1} , is reached at approximately $0.85T_m$ and is significantly lower than that of the Cr system discussed above. By contrast to Cr, the temperature dependence of the solid–liquid interface velocity can be reasonably well described by the Wilson–Frenkel expression, equation (2.1), with a single set of parameters. In fitting the results of MD simulations of the crystallization front propagation for Si (shown by dark diamonds in figure 2b), we use the temperature dependences of the atomic self-diffusivity in liquid phase $D(T)$ and latent heat of melting $\Delta H(T)$ determined in an additional set of MD simulations performed under well-controlled temperature and pressure conditions at temperatures ranging from 1200 to 2000 K. Assuming $D(T) = D_0 \exp(-Q_h/k_B T)$ and $C_h(T) = C_0 D_0 \exp(-\Delta H(T)/k_B T_m)$, equation (2.1) can then be rewritten as follows:

$$V(T) = C_0 D(T) \left[\exp\left(-\frac{\Delta H(T)}{k_B T_m}\right) - \exp\left(-\frac{\Delta H(T)}{k_B T}\right) \right]. \quad (2.3)$$

The only fitting parameter, a constant pre-factor $C_0 = 1.12 \times 10^{11} \text{ m}^{-1}$, is fitted to the melting front velocities at 1800 K, 1900 K and 2000 K predicted from the crystal–liquid coexistence MD simulations described above, as shown in the inset of figure 2b. The interface velocities predicted by equation (2.3) are plotted as red dots connected by the red line in figure 2b. Even though the crystallization front velocities calculated in MD simulations are not used in the fitting of equation (2.3), they are still described reasonably well by the kinetic equation. For temperatures lower than approximately $0.7T_m$, the solidification velocity approaches zero and the analysis of the atomic structure reveals the transformation of the supercooled liquid to the amorphous state. We note that the temperature dependence of the liquid phase atomic diffusion, $D(T)$, is found to exhibit a non-Arrhenius dependence at strong levels of undercooling, with the effective diffusion barrier changing from 0.49 eV fitted in the temperature range of $0.89T_m < T < 1.19T_m$ to 2.61 eV fitted for temperatures $0.71T_m < T < 0.82T_m$.

The temperature of the transition to the amorphous state is determined from the temperature dependence of the Abraham factor g_{\min}/g_{\max} [51] calculated from the pair distribution function, where g_{\min} and g_{\max} correspond to the magnitudes of the pair distribution function at the first minimum and first maximum, respectively. The temperature dependence of the Abraham factor reflects a structural transition from an undercooled high-density high-coordinated liquid to a low-density tetrahedrally coordinated liquid [52] as the temperature decreases from $0.83T_m$ to $0.71T_m$. This transition has also been observed in other computational studies and recognized as the liquid–amorphous phase transformation [53,54]. Thus, a temperature of $0.71T_m$ is denoted as the glass transition temperature T_g of the model Si material in figure 2b.

As noted above, the strong nonlinearity of the crystallization front velocity may be related to the temperature-dependent role of relaxation processes in the vicinity of the interface, although the underlying physical mechanisms are still unclear. Phenomenologically, the role of the relaxation processes in crystal growth at the small and high driving forces can be described by the analysis of the solution of the kinetic PFM [34]. By introducing the relaxation of phase field (as a slow thermodynamic variable) and the relaxation of the gradient flow of phase field (as a fast thermodynamic variable), one can describe the growth of crystals modelled in atomistic simulations in various systems (Fe, Ni, Cu₅₀Zr₅₀ and Ni₅₀Al₅₀) with reasonable values of material constants and model parameters. Remarkably, when the relaxation of the gradient flow in the PFM is neglected, the growth kinetics can only be described in limited regions of undercooling (e.g. see the results of calculations in ref. [25] for crystal growth kinetics in Fe). Therefore, in addition to the Wilson–Frenkel model, equations (2.1) and (2.3), we apply the kinetic PFM to the description of the MD results for Cr and Si in the next section.

3. Phase-field model predictions

(a) The hodograph equation

Using kinetic PFM [34], the hodograph equation has been derived and solved in steady-state approximation for pure and binary systems in a manner consistent with the travelling wave solution of the PFM [30–32]. This equation takes into account relaxation of the phase field ϕ and relaxation of the gradient flow $\partial\phi/\partial t$ as independent thermodynamic variables (t stands for time), which provide description of phase transformations at small and large driving forces, respectively. Subsequently, the solution of these hyperbolic type equations yields [31,32]:

— the velocity-dependent interface width,

$$\ell(t) = \eta_{\text{int}} \left[1 - \frac{V^2(t)}{(V_\phi^B)^2} \right], \quad V(t) \leq V_\phi^B, \quad (3.1)$$

— and the hodograph equation,

$$\frac{\tau_\phi \mathcal{A}}{\left[1 - V^2/(V_\phi^B)^2 \right]^{3/2}} + \frac{V}{\left[1 - V^2/(V_\phi^B)^2 \right]^{1/2}} = \mathcal{M} \Delta G + \frac{\left[\tau_\phi (V_\phi^B)^2 \right] \kappa}{\left[1 - V^2/(V_\phi^B)^2 \right]^{1/2}}, \quad (3.2)$$

where η_{int} is the equilibrium interfacial width, V is velocity normal to the interface, V_ϕ^B is the maximum speed of the phase-field propagation in bulk phases, τ_ϕ is the relaxation time of the gradient flow $\partial\phi/\partial t$, \mathcal{A} is the acceleration of phase-field propagation, \mathcal{M} is the interface migration mobility, κ is the curvature of the interface and ΔG stands for the unified driving force presented by the difference of the Gibbs free energy: $\Delta G > 0$ defines solidification and $\Delta G < 0$ defines melting. Note that the expressions of η_{int} , \mathcal{M} and τ_ϕ depend on the used approach (effective mobility approach and kinetic energy approach) and the form of used potential (double-well or double-obstacle potentials) [31,32]. In particular, using the kinetic energy approach and double-well potential, the mobility of interface migration \mathcal{M} is given by $\mathcal{M} = v/\sigma$, and the maximum speed V_ϕ^B of the phase-field propagation can be defined as $V_\phi^B = (v/\tau_\phi)^{1/2}$, where v is the phase-field diffusion parameter and σ is the solid–liquid interface energy.

Owing to the inclusion of acceleration and high interface velocity, equation (3.2) represents a general case of a Gibbs–Thomson interfacial condition. This condition can be used in the steady-state regime with constant interface velocity ($\mathcal{A} = 0$, $V = \text{const}$ and ℓ does not depend on time), as well as in the non-stationary regimes of interface propagation ($\mathcal{A} \neq 0$ and $V \neq \text{const}$).

As the interface velocity V increases, the velocity-corrected interface thickness ℓ becomes smaller according to equation (3.1) and, in the limit of $V \rightarrow V_\phi^B$, one gets $\ell \rightarrow 0$. This limiting

case corresponds to the transition from the diffuse to the sharp interface. Otherwise, the normal velocity of the interface, V , cannot exceed the maximum speed V_ϕ^B of the propagation of a disturbance in the phase-field, $V \lesssim V_\phi^B$, as the phase field itself dictates the position of the interface, its velocity and acceleration.

(b) Steady-state regime

In the case of a planar interface rapidly propagating with a constant velocity ($V = \text{const}$ and $\kappa = 0$), the hodograph equation (3.2) gives

$$V = \frac{\mu_k(\Delta T_k)\Delta T_k}{\sqrt{1 + [\mu_k(\Delta T_k)\Delta T_k/V_\phi^B(\Delta T_k)]^2}}, \quad (3.3)$$

where μ_k is the kinetic coefficient dependent on the kinetic undercooling, ΔT_k , and the driving force ΔG has been approximated for a pure (one-component) system as $\Delta G \approx \Delta H_m \Delta T_k / T_m$ [55].

The denominator in equation (3.3) appears as the result of the relaxation of the gradient flow $\partial\phi/\partial t$, and the contribution of the square root becomes essential at high undercoolings. Indeed, as equation (3.3) predicts, the interface velocity is linearly proportional to the undercooling, $V \propto \Delta T_k$, at small levels of undercooling, i.e. when $\mu_k \Delta T_k \ll V_\phi^B$. With the increase of undercooling, the square root in denominator of equation (3.3) becomes more and more significant, which should lead to the nonlinearity and eventual decrease of the interface velocity V .

In equation (3.3), the kinetic coefficient μ_k depends on the undercooling ΔT_k as

$$\mu_k(\Delta T_k) = \frac{D_\phi(\Delta T_k)\Delta H_m}{\sigma T_m}, \quad (3.4)$$

and the maximum speed of the phase-field propagation V_ϕ^B is defined by the diffusion coefficient of the phase field D_ϕ and relaxation time of the gradient flow τ_ϕ as

$$V_\phi^B(\Delta T_k) = \sqrt{D_\phi(\Delta T_k)/\tau_\phi}. \quad (3.5)$$

In the present analysis, the relaxation time τ_ϕ is assumed to be independent of temperature, and the diffusion coefficient of phase field in equations (3.4) and (3.5) is

$$D_\phi(\Delta T_k) = D_\phi^0 \exp\left(-\frac{E_A}{T_m - \Delta T_k - T_{AB}}\right), \quad (3.6)$$

where the diffusion pre-factor D_ϕ^0 , the energy barrier E_A and the pseudo-glass transition temperature T_{AB} are the parameters of the PFM. The temperature T_{AB} controls the temperature at which a drastic change in the crystal growth kinetics may occur. For example, an abrupt drop of the interface velocity is possible at undercooling that corresponds to the temperature T_{AB} [25,34].

By substituting equation (3.6) into equation (3.5), the expression of the maximum speed of the phase-field propagation V_ϕ^B becomes

$$V_\phi^B(\Delta T_k) = V_\phi^0 \exp\left(-\frac{1}{2} \frac{E_A}{T_m - \Delta T_k - T_{AB}}\right), \quad (3.7)$$

with the pre-factor $V_\phi^0 = \sqrt{D_\phi^0/\tau_\phi}$ defining the maximum speed of the phase-field propagation.

(c) Comparison with MD simulation data

The results of MD simulations discussed for Cr and Si in §2b are related in this section to the solution of PFM, particularly, for the steady-state case, equations (3.3)–(3.7). This solution type has previously been applied to describe the MD data on the crystallization of Fe [7], Cu₅₀Zr₅₀ and Ni₅₀Al₅₀ [10] (see refs [25,32,33]). The material parameters used in PFM for Cr and Si are shown

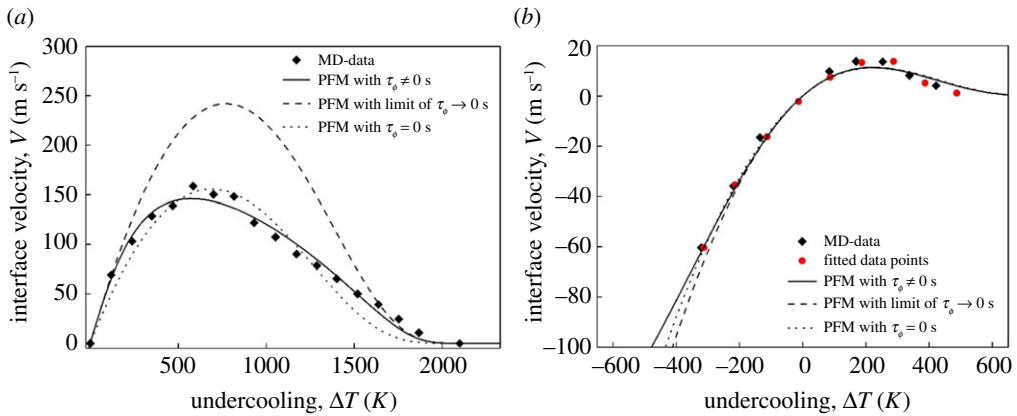


Figure 3. The dependence of crystal–liquid interface velocity on undercooling described by PFM with relaxation ($\tau_\phi \neq 0$, V_ϕ^B is finite) and PFM without relaxation ($\tau_\phi = 0$, $V_\phi^B \rightarrow \infty$) fitted to MD results (dark diamonds) for Cr (a) and Si (b). Dashed curves show the predictions of PFM without relaxation, at the limit of $\tau_\phi \rightarrow 0$ and $V_\phi^B \rightarrow \infty$, and with denominator in equation (3.3) set to unity in the calculations. The fitting for Si (b) is done to the interface velocities calculated with the Wilson–Frenkel equation, equation (2.3) (red circles [57]). Tables 1 and 2 summarize the material parameters used in the calculations for Cr and Si, respectively. (Online version in colour.)

Table 1. Material parameters of Cr used in PFM calculations.

parameter	set 0 ^a	set 1 ^a	set 2 ^a	source
latent heat, ΔH_m (J m ⁻³)	3.13×10^9	3.13×10^9	3.13×10^9	[36]
melting temperature, T_m (K)	2332	2332	2332	[38]
average solid–liquid interfacial energy, σ_0 (J m ⁻²)	0.2078	0.2078	0.2078	[56]
anisotropy parameter, ε_1	0.024	0.024	0.024	[56]
anisotropy parameter, ε_2	0.002	0.002	0.002	[56]
solid–liquid interfacial energy, $\sigma = \sigma_{001}$ (J m ⁻²) ^b	0.185	0.185	0.185	[56]
pseudo-glass transition temperature, T_{AB} (K)	0	0	0	present work
relaxation time of gradient flow, τ_ϕ (s)	0	1.48×10^{-12}	$\rightarrow 0$	present work
diffusion pre-factor, D_ϕ^0 (m ² s ⁻¹)	3.33×10^{-7}	3.29×10^{-7}	3.29×10^{-7}	present work
pre-factor, V_ϕ^0 (m s ⁻¹)	$\rightarrow \infty$	471.74	$\rightarrow \infty$	present work
energy barrier, E_A (K)	3892.35	3166.17	3166.17	present work

^aSet 0 without relaxation, set 1 with relaxation and set 2 without relaxation at the limit of $T_\phi \rightarrow 0$ and $V_\phi^B \rightarrow \infty$.

^b $\sigma_{001} = \sigma_0(1 - (18/5)\varepsilon_1 - (80/7)\varepsilon_2)$ [56].

in tables 1 and 2, respectively, where the relaxation time of gradient flow, τ_ϕ , the diffusion pre-factor, D_ϕ^0 , and the energetic barrier, E_A , are considered as free parameters at a fixed pseudo-glass transition temperature T_{AB} .

Figure 3a shows three bell-shaped curves related to the steady-state growth of Cr crystal given by equations (3.3)–(3.7) fitted to MD data for Cr for the crystallization with relaxation ($\tau_\phi \neq 0$, V_ϕ^B is finite), without relaxation ($\tau_\phi = 0$, $V_\phi^B \rightarrow \infty$), and without relaxation at a limit of ($\tau_\phi \rightarrow 0$, $V_\phi^B \rightarrow \infty$). This latter approximation corresponds to the case where the denominator (square root function) in equation (3.3), becomes equal to unity, i.e. with set 2 from table 1. Figure 3b represents the

Table 2. Material parameters of Si used in PFM calculations.

parameter	set 0 ^a	set 1 ^a	set 2 ^a	source
interfacial energy, σ (J m ⁻²)	0.0416	0.0416	0.0416	[15]
melting temperature, T_m (K)	1681	1681	1681	[37]
latent heat, ΔH_m (J m ⁻³) ^b	2.66×10^9	2.66×10^9	2.66×10^9	[57]
pseudo-glass transition temperature, T_{AB} (K)	700	700	700	present work
relaxation time of gradient flow, τ_ϕ (s)	0	2.61×10^{-13}	$\rightarrow 0$	present work
diffusion pre-factor, D_ϕ^0 (m ² s ⁻¹)	3.54×10^{-8}	4.10×10^{-8}	4.10×10^{-8}	present work
pre-factor, V_ϕ^0 (m s ⁻¹)	∞	400.2	$\rightarrow \infty$	present work
energy barrier, E_A (K)	2508.9	2621.6	2621.6	present work

^aSet 0 without relaxation, set 1 with relaxation and set 2 without relaxation at the limit of $T_\phi \rightarrow 0$ and $V_\phi^B \rightarrow \infty$.

^bArithmetic average of all values obtained for different temperatures in ref. [57].

descriptions of both crystallization and melting fitted to MD data for Si using the linear and nonlinear relationships, such as those discussed above for Cr.

The curves calculated without relaxation of gradient flow ($\tau_\phi = 0$) give the linear relationship between the interface velocity and undercooling, $V = \mu_k(\Delta T_k)\Delta T_k$. These curves fail to describe data of atomistic modelling (see dotted curve obtained with set 0 from table 1 providing the best fit to MD data of Cr). Taking into account the relaxation of gradient flow ($\tau_\phi \neq 0$), one gets a nonlinear relationship between the interface velocity and undercooling provided by equations (3.3)–(3.7) in the entire undercooling range. In this case, the MD data for Cr are well described (see solid curve in figure 3a obtained with set 1 from table 1). Otherwise, without relaxation of gradient flow ($\tau_\phi \rightarrow 0$), the solution of equations (3.3)–(3.7) can describe the MD results for Cr only at small levels of undercooling (see dashed curve in figure 3a obtained with set 2 from table 1). A similarly good agreement has also been obtained between the results of MD simulations of crystallization and melting of Si and the nonlinear equations (3.3)–(3.7) with relaxation taken into account ($\tau_\phi \neq 0$, V_ϕ^B is finite) (see solid curve in figure 3b obtained with set 1 from table 2).

The crystallization kinetics of Cr as well as melting and crystallization kinetics of Si have been well described by PFM that includes the relaxation of gradient flow as an independent thermodynamic variable in addition to the introduction of the phase field as slow thermodynamic variable. The slow phase-field variable is responsible for the description of MD data at small undercoolings, while the fast gradient flow makes it possible to account for the local non-equilibrium effects at large undercoolings. This makes the solution of the hodograph equation sufficiently flexible and enables a reliable description of the MD data in the whole range of undercoolings. The good agreement between the results of PFM calculations and MD results for Cr and Si confirms the theoretical assumption on the predominant influence of local non-equilibrium effects in crystal growth under large thermodynamic driving forces made in the derivation of the phase-field equations.

4. Summary

The results of the MD simulation study of the temperature dependence of the velocity of the crystal–liquid interface are reported for two representative one-component systems, Cr and Si. For both materials, the MD simulations predict non-monotonous dependences characterized by asymmetric bell-shaped velocity versus temperature curves. The velocities predicted in MD simulations of Si are found to be well described by the Wilson–Frenkel model adapted to account for the temperature dependences of the diffusion coefficient in the liquid phase and the latent heat of melting determined in an additional set of MD simulations. For Cr, however, a more

than three-fold reduction of the apparent diffusion activation energy upon the transition from moderate to deep (below $0.7T_m$) undercoolings makes it impossible to describe the crystallization kinetics with equations based on the diffusion-limited or collision-limited theories and a single set of parameters. The large drop of the effective activation energy observed for Cr points to a change in the dominant microscopic mechanisms responsible for the advancement of the crystallization front in the low-temperature regime.

Given the difficulties with a consistent theoretical description of the crystallization kinetics, we turn to the PFM and demonstrate that the PFM-based hodograph equation is capable of quantitative description of MD results in the whole range of temperatures. The ability of the hodograph equation to describe the results of MD simulations is related to the introduction of slow (phase field) and fast (gradient flow) variables into the original kinetic PFM. The slow phase-field variable is responsible for the description of data at small undercoolings and the fast gradient flow variable accounts for local non-equilibrium effects at high undercoolings. The introduction of these two types of variables makes the solution of the hodograph equation sufficiently flexible for a reliable description of all nonlinearities of the kinetic curves predicted in MD simulations of Cr and Si.

Data accessibility. The datasets with values of the interface velocities predicted in MD simulations for Cr and Si are provided as tables in the electronic supplementary material [58].

Authors' contributions. E.T.K., M.H. and L.V.Z. performed molecular dynamics simulations, A.S. and P.K.G. performed phase-field modelling. All authors contributed to the analysis of the results and writing the paper. All authors gave final approval for publication.

Competing interests. We declare we have no competing interests.

Funding. Funding support provided by the U.S. Department of Energy, Office of Science, Basic Energy Sciences under contract number DESC0019191 for E.T.K., M.H. and L.V.Z., and by the German Science Foundation (DFG-Deutsche Forschungsgemeinschaft) under the Project GA 1142/11-1 for P.K.G. Computational support was provided by the U.S. National Science Foundation through the Extreme Science and Engineering Discovery Environment (project TG-DMR110090).

Acknowledgements. A.S. thanks Prof. M. Bennai for hosting the present work in the research activities of LPMC.

References

1. Borisov VT. 1987 *Theory of two-phase mushy zone of metallic ingot*. Moscow, Russia: Metallurgia.
2. Chan W-L, Averback RS, Cahill DG, Ashkenazy Y. 2009 Solidification velocities in deeply undercooled silver. *Phys. Rev. Lett.* **102**, 095701. (doi:10.1103/PhysRevLett.102.095701)
3. MacDonald CA, Malvezzi AM, Spaepen F. 1989 Picosecond time-resolved measurements of crystallization in noble metals. *J. Appl. Phys.* **65**, 129. (doi:10.1063/1.342586)
4. Agranat MB, Ashitkov SI, Fortov VE, Kirillin AV, Kostanovskii AV, Anisimov SI, Kondratenko PS. 1999 Use of optical anisotropy for study of ultrafast phase transformations at solid surfaces. *Appl. Phys. A Mater. Sci. Process.* **69**, 637. (doi:10.1007/s003390051045)
5. Chen J, Chen W-K, Tang J, Rentzepis PM. 2011 Time-resolved structural dynamics of thin metal films heated with femtosecond optical pulses. *Proc. Natl Acad. Sci. USA* **108**, 18887. (doi:10.1073/pnas.1115237108)
6. Ivanov DS, Zhigilei LV. 2007 Kinetic limit of heterogeneous melting in metals. *Phys. Rev. Lett.* **98**, 195701. (doi:10.1103/PhysRevLett.98.195701)
7. Ashkenazy Y, Averback RS. 2007 Atomic mechanisms controlling crystallization behaviour in metals at deep undercoolings. *Europhys. Lett.* **79**, 26005. (doi:10.1209/0295-5075/79/26005)
8. Kerrache A, Horbach J, Binder K. 2008 Molecular-dynamics computer simulation of crystal growth and melting in $Al_{50}Ni_{50}$. *Europhys. Lett.* **81**, 58001. (doi:10.1209/0295-5075/81/58001)
9. Mendeleev MI, Rahman MJ, Hoyt JJ, Asta M. 2010 Molecular-dynamics study of solid-liquid interface migration in fcc metals. *Model. Simul. Mater. Sci. Eng.* **18**, 074002. (doi:10.1088/0965-0393/18/7/074002)
10. Tang C, Harrowell P. 2013 Anomalously slow crystal growth of the glass-forming alloy CuZr. *Nat. Mater.* **12**, 507. (doi:10.1038/nmat3631)

11. He M, Wu C, Shugaev MV, Samolyuk GD, Zhigilei LV. 2019 Computational study of short-pulse laser-induced generation of crystal defects in Ni-based single-phase binary solid–solution alloys. *J. Phys. Chem. C* **123**, 2202. (doi:10.1021/acs.jpcc.8b09922)
12. Zhong L, Wang J, Sheng H, Zhang Z, Mao SX. 2014 Formation of monatomic metallic glasses through ultrafast liquid quenching. *Nature* **512**, 177. (doi:10.1038/nature13617)
13. Ashkenazy Y, Averback RS. 2010 Kinetic stages in the crystallization of deeply undercooled body-centered-cubic and face-centered-cubic metals. *Acta Mater.* **58**, 524. (doi:10.1016/j.actamat.2009.09.030)
14. Grabow MH, Gilmer GH, Bakker AF. 1988 Molecular dynamics studies of silicon solidification and melting. *MRS Proc.* **141**, 349. (doi:10.1557/PROC-141-349)
15. Bergmann S, Albe K, Flegel E, Barragan-Yani DA, Wagner B. 2017 Anisotropic solid–liquid interface kinetics in silicon: an atomistically informed phase-field model. *Model. Simul. Mater. Sci. Eng.* **25**, 065015. (doi:10.1088/1361-651X/aa7862)
16. He M, Karim ET, Shugaev MV, Zhigilei LV. 2021 Atomistic simulation of the generation of vacancies in rapid crystallization of metals. *Acta Mater.* **203**, 116465. (doi:10.1016/j.actamat.2020.11.007)
17. Wilson HW. 1900 On the velocity of solidification and viscosity of super-cooled liquids. *Philos. Mag.* **50**, 238–250. (doi:10.1080/14786440009463908)
18. Frenkel J. 1946 *Kinetic theory of liquids*. New York, NY: Oxford University Press.
19. Turnbull D. 1962 On the relation between crystallization rate and liquid structure. *J. Phys. Chem.* **66**, 609. (doi:10.1021/j100810a009)
20. Broughton JQ, Gilmer GH, Jackson KA. 1982 Crystallization rates of a Lennard-Jones liquid. *Phys. Rev. Lett.* **49**, 1496. (doi:10.1103/PhysRevLett.49.1496)
21. Hoyt JJ, Sadigh B, Asta M, Foiles SM. 1999 Kinetic phase field parameters for the Cu–Ni system derived from atomistic computations. *Acta Mater.* **47**, 3181. (doi:10.1016/S1359-6454(99)00189-5)
22. Miroshnichenko IS. 1982 *Quenching from the liquid state*. Moscow, Russia: Metallurgia.
23. Chernov AA. 1984 *Modern crystallography III. Crystal growth*. Berlin, Germany: Springer.
24. Herlach DM, Galenko PK, Holland-Moritz D. 2007 *Metastable solids from undercooled melts*. Amsterdam, The Netherlands: Elsevier.
25. Galenko PK, Ankudinov V. 2019 Local non-equilibrium effect on the growth kinetics of crystals. *Acta Mater.* **168**, 203. (doi:10.1016/j.actamat.2019.02.018)
26. Berghoff M, Selzer M, Nestler B. 2013 Phase-field simulations at the atomic scale in comparison to molecular dynamics. *Sci. World J.* **2013**, 564272. (doi:10.1155/2013/564272)
27. Guerdane M, Berghoff M. 2018 Crystal-melt interface mobility in bcc Fe: linking molecular dynamics to phase-field and phase-field crystal modeling. *Phys. Rev. B* **97**, 144105. (doi:10.1103/PhysRevB.97.144105)
28. Jou D, Casas-Vazquez J, Lebon G. 2010 *Extended irreversible thermodynamics*, 4th edn. Dordrecht, The Netherlands: Springer.
29. Galenko P, Jou D. 2005 Diffuse-interface model for rapid phase transformations in nonequilibrium systems. *Phys. Rev. E* **71**, 046125. (doi:10.1103/PhysRevE.71.046125)
30. Galenko PK, Abramova EV, Jou D, Danilov DA, Lebedev VG, Herlach DM. 2011 Solute trapping in rapid solidification of a binary dilute system: a phase-field study. *Phys. Rev. E* **84**, 041143. (doi:10.1103/PhysRevE.84.041143)
31. Salhoumi A, Galenko PK. 2016 Gibbs–Thomson condition for the rapidly moving interface in a binary system. *Physica A* **447**, 161. (doi:10.1016/j.physa.2015.12.042)
32. Salhoumi A, Galenko PK. 2020 Fast traveling waves in the phase-field theory: effective mobility approach versus kinetic energy approach. *J. Phys. Condens. Matter* **32**, 204003. (doi:10.1088/1361-648X/ab6ae9)
33. Galenko PK, Salhoumi A, Ankudinov V. 2019 Kinetics of rapid crystal growth: phase field theory versus atomistic simulations. *IOP Conf. Ser. Mat. Sci. Eng.* **529**, 012035. (doi:10.1088/1757-899X/529/1/012035)
34. Galenko PK, Ankudinov V, Reuther K, Rettenmayr M, Salhoumi A, Kharanzhevskiy EV. 2019 Thermodynamics of rapid solidification and crystal growth kinetics in glass-forming alloys. *Phil. Trans. R. Soc. A* **377**, 20180205. (doi:10.1098/rsta.2018.0205)
35. Salhoumi A, Galenko PK. 2017 Analysis of interface kinetics: solutions of the Gibbs–Thomson-type equation and of the kinetic rate theory. *IOP Conf. Ser. Mat. Sci. Eng.* **192**, 012014. (doi:10.1088/1757-899X/192/1/012014)

36. Lin Z, Johnson RA, Zhigilei LV. 2008 Computational study of the generation of crystal defects in a bcc metal target irradiated by short laser pulses. *Phys. Rev. B* **77**, 214108. (doi:10.1103/PhysRevB.77.214108)
37. Kumagai T, Izumi S, Hara S, Sakai S. 2007 Development of bond-order potentials that can reproduce the elastic constants and melting point of silicon for classical molecular dynamics simulation. *Comput. Mater. Sci.* **39**, 457. (doi:10.1016/j.commatsci.2006.07.013)
38. Karim ET, Lin Z, Zhigilei LV. 2012 Molecular dynamics study of femtosecond laser interactions with Cr targets. *AIP Conf. Proc.* **1464**, 280. (doi:10.1063/1.4739881)
39. Luo S-N, Ahrens TJ, Çağın T, Strachan A, Goddard III WA, Swift DC. 2003 Maximum superheating and undercooling: systematics, molecular dynamics simulations, and dynamic experiments. *Phys. Rev. B* **68**, 134206. (doi:10.1103/PhysRevB.68.134206)
40. Lin Z, Leveugle E, Bringa EM, Zhigilei LV. 2010 Molecular dynamics simulation of laser melting of nanocrystalline Au. *J. Phys. Chem. C* **114**, 5686. (doi:10.1021/jp909328q)
41. Berendsen HJC, Postma JPM, van Gunsteren WF, DiNola A, Haak JR. 1984 Molecular dynamics with coupling to an external bath. *J. Chem. Phys.* **81**, 3684. (doi:10.1063/1.448118)
42. Monk J, Yang Y, Mendelev MI, Asta M, Hoyt JJ, Sun DY. 2010 Determination of the crystal-melt interface kinetic coefficient from molecular dynamics simulations. *Model Simul. Mater. Sci. Eng.* **18**, 015004. (doi:10.1088/0965-0393/18/1/015004)
43. Wu C, Zhigilei LV. 2016 Nanocrystalline and polyicosahedral structure of a nanospire generated on metal surface irradiated by a single femtosecond laser pulse. *J. Phys. Chem. C* **120**, 4438. (doi:10.1021/acs.jpcc.6b00013)
44. Buta D, Asta M, Hoyt JJ. 2007 Kinetic coefficient of steps at the Si(111) crystal-melt interface from molecular dynamics simulations. *J. Chem. Phys.* **127**, 074703. (doi:10.1063/1.2754682)
45. Jackson KA, Chalmers B. 1956 Kinetics of solidification. *Can. J. Phys.* **34**, 473. (doi:10.1139/p56-054)
46. Spaepen F, Turnbull D. 1979 Kinetics of motion of crystal-melt interfaces. *AIP Conf. Proc.* **50**, 73. (doi:10.1063/1.31738)
47. Jackson KA. 2002 The interface kinetics of crystal growth processes. *Interface Sci.* **10**, 159. (doi:10.1023/A:1015824230008)
48. Karim ET. 2016 Atomistic simulation study of short pulse laser-induced generation of crystal defects in metal targets. PhD dissertation, University of Virginia, VA.
49. Egami T, Srolovitz D. 1982 Local structural fluctuations in amorphous and liquid metals: a simple theory of the glass transition. *J. Phys. F: Met. Phys.* **12**, 2141. (doi:10.1088/0305-4608/12/10/010)
50. Mendelev MI. 2012 Molecular dynamics simulation of solidification and devitrification in a one-component system. *Model. Simul. Mater. Sci. Eng.* **20**, 045014. (doi:10.1088/0965-0393/20/4/045014)
51. Wendt HR, Abraham FF. 1978 Empirical criterion for the glass transition region based on Monte Carlo simulations. *Phys. Rev. Lett.* **41**, 1244. (doi:10.1103/PhysRevLett.41.1244)
52. Hedler A, Klaumünzer SL, Wesch W. 2004 Amorphous silicon exhibits a glass transition. *Nat. Mater.* **3**, 804. (doi:10.1038/nmat1241)
53. Sastry S, Austen Angell C. 2003 Liquid-liquid phase transition in supercooled silicon. *Nat. Mater.* **2**, 739. (doi:10.1038/nmat994)
54. Jakse N, Pasturel A. 2007 Liquid-liquid phase transformation in silicon: evidence from first-principles molecular dynamics simulations. *Phys. Rev. Lett.* **99**, 205702. (doi:10.1103/PhysRevLett.99.205702)
55. Thompson CV, Spaepen F. 1979 On the approximation of the free energy change on crystallization. *Acta Metal.* **27**, 1855. (doi:10.1016/0001-6160(79)90076-2)
56. Ueno K, Shibuta Y. 2019 Composition dependence of solid-liquid interfacial energy of Fe-Cr binary alloy from molecular dynamics simulations. *Comput. Mater. Sci.* **167**, 1–7. (doi:10.1016/j.commatsci.2019.05.023)
57. He M. 2019 Atomistic and continuum modeling of laser-induced phase transformations, generation of crystal defects, and modification of surface morphology in silicon and metal targets. PhD dissertation, University of Virginia.
58. Karim ET, He M, Salhoumi A, Zhigilei LV, Galenko PK. 2021 Kinetics of solid-liquid interface motion in molecular dynamics and phase field models: crystallization of chromium and silicon. rs.figshare.com.